

Mathematical and numerical modelling of hybrid water purification systems

Antonios Parasyris^a, Marco Discacciati^{a,*}, Diganta B. Das^b

^a Department of Mathematical Sciences, Loughborough University,
Epinal Way, Loughborough LE11 3TU, UK. {a.parasyris,m.discacciati}@lboro.ac.uk

^b Chemical Engineering Department, Loughborough University,
Epinal Way, Loughborough LE11 3TU, UK. d.b.das@lboro.ac.uk

* Corresponding author.

Abstract

We present a computational modelling framework to support the design and optimization of membrane-based water purification systems. Two modelling approaches are defined which differ in the way they describe the flow in the interfacial region between the feed domain and the membrane surface. Extensive comparison of the results obtained by the two methods highlights non-negligible differences in the predicted flow pattern, especially in the neighbourhood of the membrane. Numerical modelling and computer simulations permit to gain a deeper understanding of the flow behaviour than the sole experimental work, e.g., by identifying Dean vortices inside the feed domain and by relating them to geometrical and flow characteristics.

Keywords: Hybrid membrane filtration; Navier-Stokes equations; Porous-media flows; Dean vortices; Finite elements.

1 Introduction

The availability of clean drinking water is key for all human settlements. When natural disasters (e.g., extreme floods or earthquakes) occur, sources of drinking water may get polluted by harmful components and cannot be relied on. In such events, water purification for immediate human consumption becomes a major priority which, in many cases, must be achieved using simple ‘first-aid’ technology quickly put in place. Membrane filtration can offer a cost-effective way to treat polluted water which can be operated in simple conditions and with low energy consumption. Membranes are essentially thin sheets of porous material used to remove suspended particles from a particle-laden fluid. In [36], a novel membrane-based water purification system was proposed to address the challenges arising in a natural disaster scenario. The system exploits both a hybrid filtration technology combining standard dead-end and cross-flow filtration (see, e.g., [28]) and flow instabilities in the form of Dean vortices [12, 27] to maximize the separation rate and to minimize the fouling of the membrane [35]. Experimental work [36, 35] carried out under selected operating conditions for a specific design of this system proved its effectiveness to remove organic compounds from water. However, an in-depth understanding of both fluid-mechanical and physico-chemical aspects of the filtration process is needed to be able to optimize separation at low-power consumption as required for our target application. While the design and optimization of membrane filtration has usually heavily relied on experimental work, the development of numerical simulation techniques and computer power have made computational modelling an extremely valuable tool to complement and assist laboratory work, and dramatically reduce the amount and cost of experimental testing. The work presented in this paper constitutes a first step towards the optimization of this hybrid water purification system. Our focus here is on the fluid-dynamics aspects only and we aim to develop a reliable quantitative model that correctly describes the behaviour of the fluid both inside the feed domain and near the membrane surface. We want to identify which characteristics of the system and which operating conditions favour the development of Dean vortices and which strategies may be put in place to increase the efficiency of the filtration. A correct physical modelling of the water purification device requires introducing different systems of partial differential equations in the region occupied by the feed (free-fluid region) and in the one formed by the membrane that we model as a uniform isotropic porous medium. This leads

to a heterogeneous problem governed by partial differential equations of different order. While the (second order) Navier-Stokes equations are certainly suitable to describe the motion of incompressible flows in the free-fluid region, the choice of an appropriate model for flows through a saturated membrane depends both on the characteristics of the latter and on the fluid regime. In fact, the classical (first order) Darcy's law [10] may not accurately represent flows at large Reynolds numbers and other models such as (the second order) Brinkman's equation [8] should be considered. Suitable conditions for coupling free and porous flow must complete the definition of these heterogeneous models to correctly describe filtration. A precise representation of the fluid on the membrane surface is indeed crucial to identify and prevent situations that may lead to fouling. Several modelling approaches have been proposed where free and porous-medium flow regimes are either separated by an ideal interface (see, e.g., [5, 39, 24, 32]) or by a suitable boundary-layer transition region (see, e.g., [26, 19]). To avoid the difficulties associated with analysing and implementing heterogeneous models, a different approach similar to the so-called fictitious domain method (see, e.g., [2, 25]) and especially popular in CFD software uses a modified form of the Navier-Stokes equations in the whole computational domain and the porous medium is described by ad-hoc resistance terms.

In this paper, we formulate the Navier-Stokes-Darcy, the Navier-Stokes-Brinkman and the one-domain methods for the application of our interest, and we introduce their finite element approximations. We discuss how to implement them in a widely used commercial software and we simulate numerically different configurations of the hybrid filtration system. We compare the two modelling approaches especially in the region neighbouring the membrane surface where filtration takes place. The configuration of the water purification system introduces additional computational challenges due both to the presence of different geometrical scales between the fluid and the porous-medium regions and to centripetal forces in the feed domain that give rise to Dean vortices. We characterize the latter in terms of the dimensionless Dean number and of the aspect ratio of the fluid domain and we propose an alternative configuration to the original design of the system that better favours the onset and persistence of these secondary flows at lower energy consumption.

The paper is organized as follows. Section 2 describes the water purification system and introduces our modelling assumptions. The mathematical models together with their coupling and boundary conditions are presented in section 3. Finally, section 4 discusses the finite element approximation, presents simulation results and provides some indications towards the optimization of the system.

2 The water purification system: description and modelling assumptions

We consider a water purification system made by a sample cylindrical reservoir of radius 0.045 m filled with unfiltered water (feed) up to height $H = 0.1$ m and by a membrane-based filter fitted at the bottom of the reservoir that removes impurities and lets purified water (permeate) through. The membrane has porosity (i.e., the fraction of volume of the voids to the total volume of the membrane) $\epsilon_p = 0.54$, radius 0.045 m and thickness (after wetting) $2.73\text{e-}4$ m, approximately one third of the depth of the spiral channels which is $7.6\text{e-}4$ m [36]. The feed enters the filter through an inlet nozzle, and a peristaltic pump recirculates the retentate back into the reservoir as schematically illustrated in Fig. 1. A pressure gradient to enhance filtration is created by injecting pressurized gas into the reservoir in a uniform controlled way.

The filter has been designed to force the feed to move along a spiral-shaped channel with impermeable upper and lateral walls placed on a thin permeable membrane which is kept in place by a bottom plate where the permeate is collected. The spiral channels are clearly visible in Fig. 1 (a) and a schematic representation of the system in the neighbourhood of the inlet nozzle is shown in Fig. 2.

The filter exploits a hybrid filtration concept that combines the advantages of both dead-end and crossflow filtration methods. The former enables rapid separation because the feed is forced

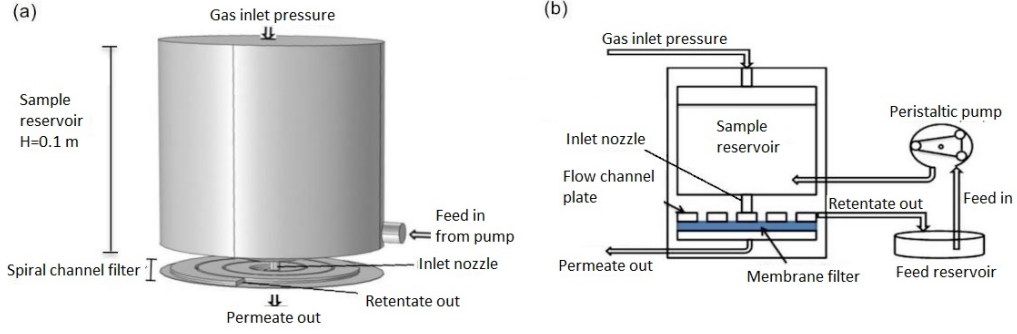


Figure 1: (a) 3D representation of the sample reservoir and spiral channel filter. (b) 2D schematic representation of the filtration system.

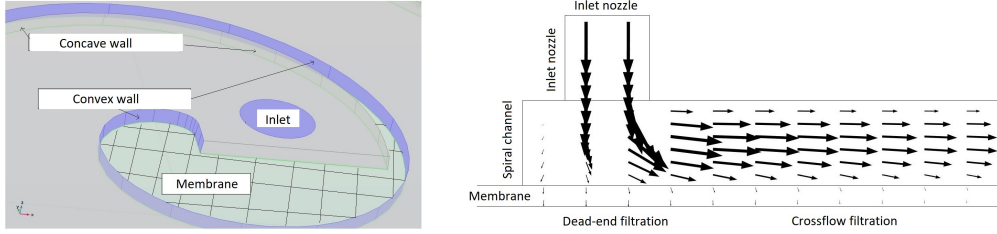


Figure 2: 3D representation of the system close to the inlet nozzle (left) and 2D cross section (right).

perpendicularly against the surface of the membrane, while the latter induces a slower separation but the retentate keeps moving along the flow direction tangentially to the membrane thus reducing the blocking of the pores due to impurities. In reference to the system, dead-end filtration mainly occurs close to the inlet nozzle while crossflow filtration takes place all along the spiral channel where the flow is mostly tangential to the membrane surface (see Fig. 2). Moreover, at sufficiently high Reynolds number, the centrifugal and centripetal forces exerted on the fluid due to the curved shape of the channels are expected to give rise to Dean vortices (see, e.g., [12, 6]) that, by creating a secondary flow from the convex towards the concave wall of the channel, may aid filtration by mixing the feed and by disrupting solute build-up on the membrane surface (see, e.g., [17]). Experimental evidence that this hybrid filtration technique maximizes the permeate flux, has higher rejection rates and is more cost effective than alternative stirred dead-end filtration methods was provided in [35, 36].

In this work, we model the feed as a single-phase incompressible viscous flow neglecting the presence of impurities with the aim of identifying suitable numerical models for the steady-state hydrodynamic behaviour of the system and to replicate experiments where clean water was used. We observe that the fluid completely fills the spiral channels so that no free surface has to be considered therein. Finally, we use suitable boundary conditions both to model the hydrostatic pressure due to the feed in the reservoir and to describe the peristaltic pump and the outflow bottom plate.

3 Mathematical modelling

In this section, we present two possible modelling approaches for the water filtration process in the system introduced in section 2. The models are based on systems of partial differential equations to describe the flow inside the spiral channel and through the membrane, and they include suitable boundary conditions to represent the remaining components of the system. As shown in Fig. 3, we

denote by Ω_f the domain formed by the spiral channel where the fluid flows above the membrane, say Ω_p . These two regions are non-intersecting and separated by a common surface (interface) Γ_I : $\Omega_f \cap \Omega_p = \emptyset$, $\Gamma_I = \overline{\Omega_f} \cap \overline{\Omega_p}$. The fluid in Ω_f is water characterized by density $\rho = 1\text{e}3 \text{ kg/m}^3$ and dynamic viscosity $\mu = 1\text{e}-3 \text{ Pas}$. We denote by \mathbf{u} and p the velocity and pressure of the fluid, respectively, and by the subscripts either f or p we indicate if a variable is defined either in Ω_f or in Ω_p . Variables without any subscript are understood to be defined for both the domains.

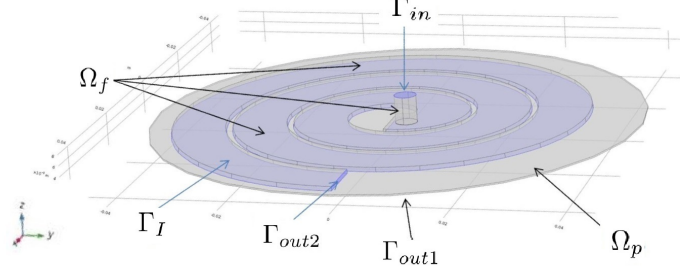


Figure 3: Representation of the computational domain formed by the fluid channel Ω_f and by the membrane Ω_p .

3.1 Coupled heterogeneous models

A possible way to describe the filtration system consists of adopting different sets of equations in Ω_f and Ω_p to account for the different flow physics in these two regions: free flow in Ω_f and porous-medium flow in Ω_p . These equations must be coupled through suitable sets of conditions across the interface Γ_I to represent filtration. More precisely, in Ω_f , we consider the incompressible Navier-Stokes equations: find \mathbf{u}_f and p_f such that

$$\begin{aligned} \rho(\mathbf{u}_f \cdot \nabla) \mathbf{u}_f &= \nabla \cdot \mathbf{T}(\mu; \mathbf{u}_f, p_f) + \rho \mathbf{g} & \text{in } \Omega_f, \\ \nabla \cdot \mathbf{u}_f &= 0 & \text{in } \Omega_f, \end{aligned} \quad (1)$$

where \mathbf{g} is the gravity acceleration, while $\mathbf{T}(\mu; \mathbf{u}_f, p_f) = -p_f \mathbf{I} + \mu(\nabla \mathbf{u}_f + (\nabla \mathbf{u}_f)^T)$ is the Cauchy stress tensor.

In the porous medium Ω_p , one could consider either Darcy's law or Brinkman's equation. Darcy's law provides the simplest linear relation between velocity and pressure drop for an incompressible fluid in a saturated porous medium [10]:

$$\begin{aligned} \mathbf{u}_p &= -\frac{\mathbf{K}}{\mu}(\nabla p_p - \rho \mathbf{g}) & \text{in } \Omega_p, \\ \nabla \cdot \mathbf{u}_p &= 0 & \text{in } \Omega_p, \end{aligned} \quad (2)$$

with \mathbf{K} the permeability tensor. If the porous medium is homogeneous and isotropic as in our case, we can replace \mathbf{K} by a constant K that, for our applications is $4.99\text{e}-15 \leq K \leq 2.83\text{e}-14 \text{ m}^2$. Darcy's law is generally considered valid if the Reynolds number Re_p inside the porous medium (computed considering as characteristic length the average pore radius) is below 10. Since the average pore diameter of the membrane we consider is approximately $1\text{e}-7 \text{ m}$ [36], $Re_p \approx 0.11 U_p$, with U_p the characteristic velocity in the porous domain. Thus, we can use Darcy's law (2) up to average velocities of about 9 m/s , a value well above our measured experimental values. However, the porosity of the membrane is close to the threshold value 0.6 above which shear stresses inside the porous medium are generally considered to become non-negligible (see, e.g., [9, 29]). In such cases, Darcy's law is normally replaced by Brinkman's equation [8].

This equation introduces a correction to the Navier-Stokes momentum equation through the Darcian term $\mu K^{-1} \mathbf{u}_p$ to mimic the presence of a porous medium. The resulting momentum equation

has the same order than Navier-Stokes' and, together with the continuity equation, reads: find \mathbf{u}_p and p_p such that

$$\begin{aligned} \rho(\mathbf{u}_p \cdot \nabla) \mathbf{u}_p &= \nabla \cdot \mathbf{T}(\mu_b; \mathbf{u}_p, p_p) - \mu K^{-1} \mathbf{u}_p + \rho \mathbf{g} & \text{in } \Omega_p, \\ \nabla \cdot \mathbf{u}_p &= 0 & \text{in } \Omega_p. \end{aligned} \quad (3)$$

Equation (3)₁ involves the so-called effective (or Brinkman) viscosity μ_b instead of μ , which should be estimated experimentally [16] but is commonly approximated as $\mu_b \approx \mu$ [40].

If we consider the Navier-Stokes equations (1) in Ω_f and either Darcy's law (2) or Brinkman's equation (3) in Ω_p , we must introduce suitable coupling conditions between these models in order to correctly represent flow behaviour across the interface Γ_I .

To couple Navier-Stokes and Darcy equations, a classical set of conditions (see, e.g., [5, 34, 24, 15]) prescribes the continuity of the normal velocity (as a consequence of the incompressibility of the fluid):

$$\mathbf{u}_f \cdot \mathbf{n} = \mathbf{u}_p \cdot \mathbf{n} \quad \text{on } \Gamma_I; \quad (4)$$

the balance of the normal stresses:

$$p_p + \rho g z = -\mathbf{n} \cdot \mathbf{T}(\mu; \mathbf{u}_f, p_f) \cdot \mathbf{n} \quad \text{on } \Gamma_I, \quad (5)$$

where z is the elevation with respect to a reference level, $g = |\mathbf{g}|$, and the so-called Beavers-Joseph-Saffman (BJS) condition for the Navier-Stokes tangential velocity:

$$\mathbf{t} \cdot \mathbf{T}(\mu; \mathbf{u}_f, p_f) \cdot \mathbf{n} = -\mathbf{t} \cdot \left(\frac{\alpha \mu}{\sqrt{K}} \mathbf{u}_f \right) \quad \text{on } \Gamma_I. \quad (6)$$

Here, \mathbf{n} and \mathbf{t} are the normal and tangential unit vectors on Γ_I with \mathbf{n} pointing outwards of Ω_f , and α is the non-dimensional BJS slip coefficient that depends on the characteristics of the porous medium [5]. Notice that the tangential velocity may be discontinuous across Γ_I .

To couple Navier-Stokes and Brinkman's equations, some authors impose the continuity of both velocity and normal stress (see, e.g., [30, 21]):

$$\begin{aligned} \mathbf{u}_p &= \mathbf{u}_f & \text{on } \Gamma_I \\ \mathbf{T}(\mu_b; \mathbf{u}_p, p_p) \cdot \mathbf{n} &= \mathbf{T}(\mu; \mathbf{u}_f, p_f) \cdot \mathbf{n} & \text{on } \Gamma_I, \end{aligned} \quad (7)$$

while others replace (7)₂ by a jump condition for the tangential component of the stress (see, e.g., [39]):

$$(\epsilon_p^{-1} \nabla \mathbf{u}_p - \nabla \mathbf{u}_f) \cdot \mathbf{n} = \frac{\beta}{\sqrt{K}} \mathbf{u}_p \quad \text{on } \Gamma_I,$$

where ϵ_p is the porosity of the porous medium and β is a dimensionless coefficient to be determined experimentally.

3.2 One-domain approach

The difficulty of identifying proper coupling conditions on Γ_I and of solving different type of equations in Ω_f and Ω_p is avoided by the so-called one-domain approach [26]. This technique, commonly implemented in commercial finite element software (such as, e.g., COMSOL Multiphysics [22]), uses a unified momentum equation in $\Omega = \Omega_f \cup \Omega_p$ with a space-dependent porosity and a characteristic function that multiplies the Darcian term introduced in (3) so that the latter vanishes in Ω_f . More precisely, the momentum equation proposed in [26] reads: find \mathbf{u} and p in Ω such that

$$\begin{aligned} \rho \left(\frac{\mathbf{u}}{\epsilon_p} \cdot \nabla \right) \frac{\mathbf{u}}{\epsilon_p} &= \nabla \cdot \mathbf{T}(\mu_b \epsilon_p^{-1}; \mathbf{u}, p) - \mu \tilde{K} \mathbf{u} + \rho \mathbf{g} & \text{in } \Omega, \\ \nabla \cdot \mathbf{u} &= 0 & \text{in } \Omega, \end{aligned} \quad (8)$$

where the porosity ϵ_p is set equal to 1 in Ω_f , \tilde{K} is zero in Ω_f and $\tilde{K} = K^{-1}$ in Ω_p . This model ensures the continuity of \mathbf{u} and p across the interface Γ_I but it induces an interfacial stress jump due both to the discontinuous porosity and to the Darcian term that gives an additional stress inside the porous medium domain. (Model (8) is often referred to as ‘Brinkman model’ due to its formal similarity with Brinkman’s equation (3).)

A theoretical comparison between the Navier-Stokes/Darcy (NSD) model and the one-domain approach is carried out in [26] considering a 2D Poiseuille flow over a porous layer similarly to Beaver and Joseph’s experiment [5]. In particular, we point out that the continuity of \mathbf{u} across Γ_I results in a smaller velocity in Ω_f than the one estimated by the NSD model, as we will also observe numerically for our problem (see section 4.2).

3.3 Boundary conditions and well-posedness

The models introduced in sections 3.1 and 3.2 must be supplemented with suitable boundary conditions to represent the feed reservoir, the outflow of the permeate and the presence of the peristaltic pump. To describe the fluid inflow into the nozzle Γ_{in} from the reservoir subject to a prescribed pressure, we impose

$$\begin{aligned} \mathbf{n} \cdot \mathbf{T}(\mu; \mathbf{u}_f, p_f) \cdot \mathbf{n} &= -(p_{atm} + p_{in} + \rho g(H + z_{in})) \quad \text{on } \Gamma_{in}, \\ \mathbf{u}_f \cdot \mathbf{t} &= \mathbf{0} \quad \text{on } \Gamma_{in}. \end{aligned} \quad (9)$$

Here p_{atm} is the atmospheric pressure, p_{in} is the pressure due to injected pressurized gas through the gas inlet (see Fig. 1), and the last term in (9)₁ represents the hydrostatic pressure induced by the constant water level H in the reservoir, with z_{in} the elevation of Γ_{in} with respect to the reference level $z = 0$ located at Γ_{out1} .

The peristaltic pump is described through the outflow boundary conditions

$$\begin{aligned} \mathbf{n} \cdot \mathbf{T}(\mu; \mathbf{u}_f, p_f) \cdot \mathbf{n} &= -(p_{atm} + \rho g z) \quad \text{on } \Gamma_{out2}, \\ \mathbf{u}_f \cdot \mathbf{t} &= \mathbf{0} \quad \text{on } \Gamma_{out2}. \end{aligned} \quad (10)$$

On the remaining boundary $\Gamma_f = \partial\Omega_f \setminus (\Gamma_{in} \cup \Gamma_{out2} \cup \Gamma_I)$, we impose the no-slip condition

$$\mathbf{u}_f = \mathbf{0} \quad \text{on } \Gamma_f. \quad (11)$$

Boundary conditions (9)-(11) apply both to the Navier-Stokes equations (1) and to the one-domain model (8), that indeed coincide in Ω_f .

As concerns the boundary conditions for the porous medium domain, we distinguish two cases. On the one hand, if Darcy’s law (2) is used in Ω_p , we impose

$$p_p = p_{atm} \quad \text{on } \Gamma_{out1}, \quad (12)$$

while on the remaining boundary $\Gamma_p = \partial\Omega_p \setminus (\Gamma_{out1} \cup \Gamma_I)$, we set

$$\mathbf{u}_p \cdot \mathbf{n} = 0 \quad \text{on } \Gamma_p. \quad (13)$$

On the other hand, if either Brinkman equations (3) or the one-domain model (8) are considered in Ω_p , we impose:

$$\begin{aligned} \mathbf{n} \cdot \mathbf{T}(\mu_*; \mathbf{u}_*, p_*) \cdot \mathbf{n} &= -p_{atm} \quad \text{on } \Gamma_{out1}, \\ \mathbf{u} \cdot \mathbf{t} &= \mathbf{0} \quad \text{on } \Gamma_{out1}, \\ \mathbf{u} &= \mathbf{0} \quad \text{on } \Gamma_p, \end{aligned} \quad (14)$$

with $\mathbf{T}(\mu_*; \mathbf{u}_*, p_*) = \mathbf{T}(\mu_b; \mathbf{u}_p, p_p)$ for (3) and $\mathbf{T}(\mu_*; \mathbf{u}_*, p_*) = \mathbf{T}(\mu_b \epsilon_p^{-1}; \mathbf{u}, p)$ for (8).

The well-posedness of the NSD and of the one-domain models have been studied in [4, 18] and [23], respectively, under suitable hypotheses on the data of the problem. For the coupled model formed by the Brinkman and Stokes equations (instead of Navier-Stokes) with suitable coupling conditions, we refer to [3].

Summarizing, we have formulated three possible mathematical models to describe the water purification system of section 2: the NSD model (1)-(2) with coupling conditions (4)-(6) and boundary conditions (9)-(13); the Navier-Stokes-Brinkman model (1), (3) with coupling conditions (7) and boundary conditions (9)-(11) and (14); and the one-domain model (8) with boundary conditions (9)-(11) and (14).

We want to compare numerically the two modelling approaches (heterogeneous versus one-domain) for the simulation of our filtration system. To this aim, we focus on the NSD and the one-domain models to investigate the impact of using either Darcy or Brinkman equations in Ω_p and of adopting either the coupling conditions (4)-(6) or the discontinuous coefficients as in (8) to represent the flow in the neighbourhood of the interface Γ_I .

4 Numerical results

In this section, we study numerically the behaviour of the filtration system of section 2 by approximating the solutions of the NSD and of the one-domain models by the finite element method. The simulations were obtained using COMSOL Multiphysics 5.3a [22] on a PC with Intel i7-6700K CPU and 64 GB RAM.

4.1 Discretization and test configurations

As the computational domain is characterized by different characteristic lengths, we consider an anisotropic mesh made of tetrahedra and prisms refined both inside the spiral channel and in the membrane domain directly below the channel, where we expect the most significant features of the flow to occur. In the rest of the porous-medium domain, the fluid velocity is expected to be very small and with little variations also in the pressure field, so that a coarser mesh is adopted as shown in Fig. 4(a), (b).

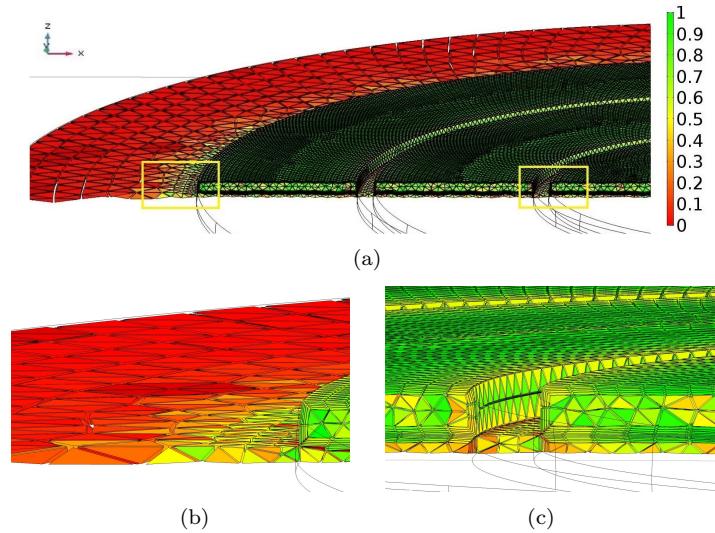


Figure 4: (a) Computational mesh with local refinement inside Ω_f and in the adjacent region to Ω_p . The colourbar indicates the skewness of the elements. (b) Zoom in the left box in (a) showing the refinement and the anisotropic elements in the membrane away from the spiral channel. (c) Zoom in the right box in (a) showing the boundary layers on Γ_f and across the interface Γ_I .

The anisotropy of the mesh is quantified through the skewness S of each element

$$S = 1 - \max_{i=1,\dots,N_a} \left(\frac{\theta_i - \theta_e}{\pi - \theta_e}, \frac{\theta_e - \theta_i}{\theta_e} \right),$$

where θ_i ($i = 1, \dots, N_a$) are the angles of each element and θ_e is the angle of the corresponding edge or vertex in an ideal element. Values of S close to 1 indicate (almost) uniform elements while low values of S denote distorted elements. The lowest value supported by COMSOL Multiphysics is $S = 0.01$ and, in our mesh, the minimum S is 0.05.

We generate two computational meshes including the features discussed above with increasing number of elements as indicated in table 2 and we compare the solutions obtained on the two meshes.

For the finite element approximation of both the NS and the one-domain equations we considered $\mathbb{P}_1 - \mathbb{P}_1$ elements with streamline stabilization [7, 20, 37]. As concerns Darcy's problem (2), COMSOL automatically solves it as the elliptic equation for the pressure: find p_p such that

$$\nabla \cdot \left(-\frac{K}{\mu} \nabla p_p \right) = 0 \quad \text{in } \Omega_p, \quad (15)$$

and then it uses Darcy's law (2)₁ to post-process the velocity. The pressure p_p is discretized using \mathbb{P}_1 Lagrangian elements. Notice that, since COMSOL uses (15) instead of the mixed formulation (2), the system arising from the discretization of the NSD model has less unknowns (degrees of freedom) than the one associated with the one-domain model (see table 2).

Concerning the coupling conditions for the NSD model, we remark that the BJS condition (6) and the continuity of normal stresses (5) should be implemented as boundary stresses for (1). More precisely, in our setting and letting $\mathbf{u}_f = (u_f, v_f, w_f)^T$, this corresponds to

$$\mathbf{T}(\mu; \mathbf{u}_f, p_f) \cdot \mathbf{n} = \left(-u_f \frac{\alpha\mu}{\sqrt{K}}, -v_f \frac{\alpha\mu}{\sqrt{K}}, p_p + \rho g z \right)^T \quad \text{on } \Gamma_I. \quad (16)$$

Then, for (15) we impose the continuity of normal velocities (4) as a Neumann boundary condition for the pressure. (Alternatively, one could impose (4) and (6) for (1), and (5) for (2). However, this approach may give non-physical results especially in the neighbourhood of the interface. This might be due to the fact that Darcy's velocity is only computed as a post-processed variable leading to incorrectly impose the continuity of normal velocities across Γ_I , while the previous strategy uses only variables actually computed at each iteration.)

To solve the non-linear systems arising from the finite element discretization, we used two solvers available in COMSOL Multiphysics 5.3a: either the Double Dogleg iterative method (a trust-region algorithm that combines Newton's method and steepest descent [13]) or the highly-non-linear (HNL) Newton method [14]. Finally, the linearized systems obtained at each iteration are solved by the direct multifrontal method MUMPS [1].

We focus on three experimental configurations characterized by different inflow pressure p_{in} and membrane permeability K as indicated in table 1.

Table 1: Configurations of interest.

Configuration	C1	C2	C3
p_{in} (Pa)	1e3	1e4	1e5
Permeability K (m ²)	2.83e−14	8.84e−15	4.99e−15

Notice that the inflow pressures considered here are significantly lower than those normally employed, e.g., in industrial settings. This is due to the application we target, i.e., water treatment in emergency situations such as natural disasters where high pressures cannot be achieved due to lack of equipment [36]. The values of K have been obtained experimentally and they decrease for increasing p_{in} due to membrane compaction (see, e.g., [33]), i.e., they tend to a limiting value corresponding to the situation of maximum compaction of the membrane pores due to the applied pressure.

Table 2 reports the number of iterations to achieve the tolerance $tol = 1e-3$ for the residual and the computational time. (Here, the BJS coefficient for the NSD model is set to $\alpha = 1$.) We

can see that the Dogleg method is robust with respect both to the number of degrees of freedom (dofs) and to increasing inflow pressure for the first two configurations but it does not converge for configuration C3. HNL Newton converges in all cases but with a much higher computational cost. The behaviour of the two methods suggests that more advanced solution techniques should be employed, e.g., ad-hoc preconditioning. We also observe that NSD requires lower computational time with respect to the one-domain model due to fewer dofs involved at each iteration.

Table 2: Iterations and computational time for the two meshes and models. (‘-’ indicates that the method did not converge to the required tolerance.)

		Mesh 1		Mesh 2	
		659,139		1,223,529	
		NSD	One-domain	NSD	One-domain
No. elements:	Model:	829,852	1,080,036	1,531,330	1,973,072
No. dofs:					
Double Dogleg iterations for configuration	C1	9	8	10	11
	C2	12	13	23	17
	C3	-	-	-	-
Double Dogleg computational time (min) for configuration	C1	11	14	18	47
	C2	15	24	43	72
	C3	-	-	-	-
HNL Newton iterations for configuration	C1	39	38	37	38
	C2	83	85	105	146
	C3	75	98	103	98
HNL Newton computational time (min) for configuration	C1	57	99	70	190
	C2	121	222	199	730
	C3	136	420	351	709

Let now \mathbf{u}_*^i, p_*^i be the vectors of the computed nodal values of velocity and pressure using mesh $i = 1, 2$ for Navier-Stokes ($* = f$), Darcy ($* = p$) or the one-domain model (no subscript). We compute the relative errors:

$$e_*^u = \frac{\|\mathbf{u}_*^1 - \mathbf{u}_*^2\|}{\|\mathbf{u}_*^2\|} \quad \text{and} \quad e_*^p = \frac{\|p_*^1 - p_*^2\|}{\|p_*^2\|},$$

where $\|\cdot\|$ is the Euclidean norm of the computed/interpolated values of velocity and pressure at the nodes of the union of the two meshes. The relative errors reported in table 3 show that the pressure is computed accurately by Mesh 1 and the relative errors for the velocity e_f^u and e^u do not exceed 6.38%. We also observe that the highest relative error is for Darcy’s velocity, which is expected since this is a post-processed quantity and, due to the post-processing procedure, additional errors are generated. Considering the errors of table 3 and the computational times of table 2, we choose Mesh 1 as a convenient discretization for the numerical simulation of the filtration system.

Table 3: Relative errors for configurations C1–C3.

Relative errors		e_f^u	e_f^p	e_p^u	e_p^p	e^u	e^p
Configuration	C1	6.37e-2	2.28e-5	1.36e-1	2.92e-4	6.38e-2	3.16e-4
	C2	4.55e-2	6.41e-4	1.37e-1	1.58e-3	4.55e-2	1.74e-3
	C3	3.87e-2	6.94e-3	1.49e-1	1.22e-2	3.97e-2	1.30e-2

Finally, we observe that the numerical scheme guarantees a good conservation of mass. Indeed, let Γ be one of the inflow/outflow boundaries Γ_{in} , Γ_{out1} or Γ_{out2} and \mathbf{u}_* the fluid velocity computed

using one of the models. The flux (m^3s^{-1}) through Γ is defined as

$$F(\Gamma) = \int_{\Gamma} \mathbf{u}_* \cdot \mathbf{n} d\Gamma.$$

Then, taking, e.g., configuration C2, for the NSD model ($\alpha = 1$) we have $F(\Gamma_{in}) = -6.68\text{e-}6 \text{ m}^3\text{s}^{-1}$, $F(\Gamma_{out1}) = 6.30\text{e-}7 \text{ m}^3\text{s}^{-1}$ and $F(\Gamma_{out2}) = 6.05\text{e-}6 \text{ m}^3\text{s}^{-1}$, while for the one-domain model $F(\Gamma_{in}) = -6.71\text{e-}6 \text{ m}^3\text{s}^{-1}$, $F(\Gamma_{out1}) = 6.87\text{e-}7 \text{ m}^3\text{s}^{-1}$ and $F(\Gamma_{out2}) = 6.02\text{e-}6 \text{ m}^3\text{s}^{-1}$, so that, in both cases, $|F(\Gamma_{in} \cup \Gamma_{out1} \cup \Gamma_{out2})| \leq 3.83\text{e-}9 \text{ m}^3\text{s}^{-1}$. The numerical fluxes through Γ_{out1} are in good agreement with the experimental data obtained in laboratory as shown in table 4.

Table 4: Experimental and numerical flux $F(\Gamma_{out1})$ (m^3s^{-1}).

Configuration	C1	C2	C3
Experimental	2.19e-7	6.84e-7	3.87e-6
NSD	3.81e-7	6.30e-7	2.76e-6
One-domain	4.13e-7	6.87e-7	3.03e-6

4.2 Comparison between the NSD and the one-domain models

In this section, we compare the velocity and pressure fields computed using the one-domain and the NSD models with different values of the BJS coefficient α . We plot the results on three horizontal planes parallel to $z = 0$ (see Fig. 5): $z = 6.53\text{e-}4 \text{ m}$ in the middle of the spiral channel, $z = 2.73\text{e-}4 \text{ m}$ on the interface Γ_I , and $z = 1.365\text{e-}4 \text{ m}$ in the middle of the porous medium domain, and also on the cross sections S1-S3 to highlight some features of the flow.

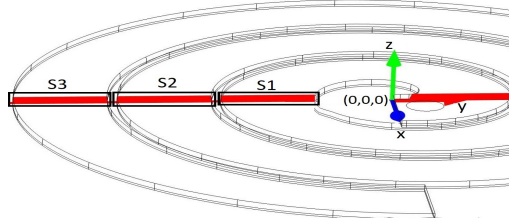


Figure 5: Reference system and cross sections S1-S3. The plane $z = 0$ coincides with the bottom face of the membrane (outflow boundary Γ_{out1}).

Concerning the role of α , we expect lower values of this parameter to correspond to higher interfacial tangential (slip) velocity since, according to (6), the interfacial tangential stress should decrease. Thus, reducing α , the outward flux through Γ_{out2} should increase while the one through Γ_I should decrease. Numerical results for configuration C2 reported in table 5 confirm the expected trend although the variation in the normal flux $F(\Gamma_I)$ is in fact very small. We choose $\alpha = 0.1$ and $\alpha = 1$ to study the impact of the BJS slip coefficient on numerical simulations. These values provide physically significant bounds for the value of α that one could estimate for our membrane using Saffman's experimental relationship [34, 11]: $\alpha = (5\sqrt{\epsilon_p})^{-1} = (5\sqrt{0.54})^{-1} \approx 0.27$.

While the computed absolute pressure and normal velocity at the interface Γ_I do not present significant variations between NSD (either with $\alpha = 0.1$ or $\alpha = 1$) and the one-domain model, remarkable differences can be noticed for the tangential velocity, as shown in Fig. 6. In fact, the average magnitude of the computed tangential velocity component at the interface is approximately $9.8\text{e-}5$ for the one-domain model, $8.6\text{e-}4$ for NSD with $\alpha = 1$ and $8.6\text{e-}3$ for NSD with $\alpha = 0.1$. As anticipated in section 3, this is due to the fact that, while the NSD tangential velocity may be discontinuous across the interface, the continuity imposed by the one-domain model implies that

Table 5: Flux through Γ_{out1} , Γ_{out2} and Γ_I for different values of α .

α	$F(\Gamma_{out1})$	$F(\Gamma_{out2})$	$F(\Gamma_I)$
0.001	5.97e-7	7.67e-6	6.17e-7
0.1	6.26e-7	6.08e-6	6.47e-7
1	6.30e-7	6.05e-6	6.50e-7
3	6.30e-7	6.04e-6	6.51e-7

velocity on Γ_I must match the corresponding low value characterizing the porous medium. (For configurations C1 and C3 a similar behaviour is observed.)

On the one hand, our results highlight the importance of correctly estimating the BJS parameter α to guarantee the reliability of the results provided by the NSD model. On the other hand, they suggest that membranes manufactured to have low values of α may feature lower build-up on their filtration surface than generic membranes due to increased interfacial tangential stress resulting from higher tangential velocity.

In the middle of the membrane and of the spiral fluid channel, no significant differences can be noticed between the modelling approaches neither for the absolute pressure nor for the velocity field as shown in Figs. 7–9.

In Fig. 8, we notice that higher values of the velocity field inside the spiral channel can be found near the concave wall. This is especially evident for the case of configuration C3 characterized by the highest value of the inflow pressure.

Moreover, plotting the absolute pressure at the cross section S1 (see Fig. 10 where, for visualization purposes, the horizontal axis has been scaled by a factor 0.15), we can see that, analogously to the tangential velocity, continuity of pressure across the interface is guaranteed only by the one-domain model while NSD results in a discontinuous pressure field across Γ_I . We also remark that a pressure gradient clearly exists between the concave and the convex walls of the channel.

Higher velocity and pressure in the neighbourhood of the concave wall indicate the presence of the expected centrifugal force due to the curved shape of the fluid channel and of the associated Dean vortices as we discuss in section 4.3. In the rest of the paper, we consider only the NSD model with $\alpha = 1$ because it provides physically significant results comparable to those obtained either setting $\alpha = 0.1$ in NSD or using the one-domain model but with lower computational cost than the latter approach.

4.3 Dean vortices

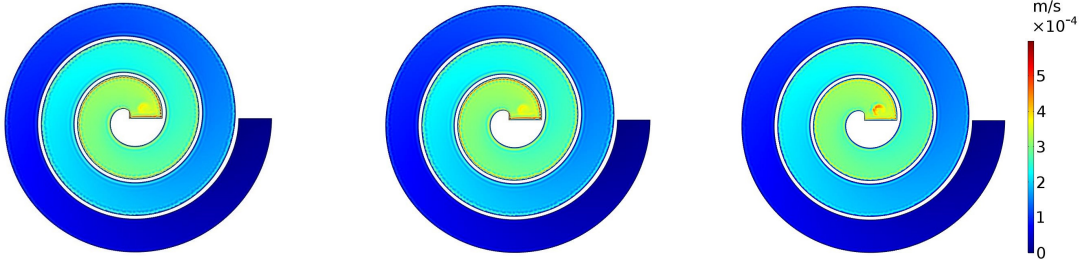
As anticipated in section 2, at sufficiently high Reynolds number, the pressure gradient created by centrifugal forces in a curved channel gives rise to a secondary flow in the form of Dean vortices. These can be characterized by the dimensionless Dean number (see, e.g., [12]) which quantifies the ratio of the centrifugal force to the viscous force and can be defined as

$$De = Re \sqrt{\frac{D_h}{2R}}, \quad (17)$$

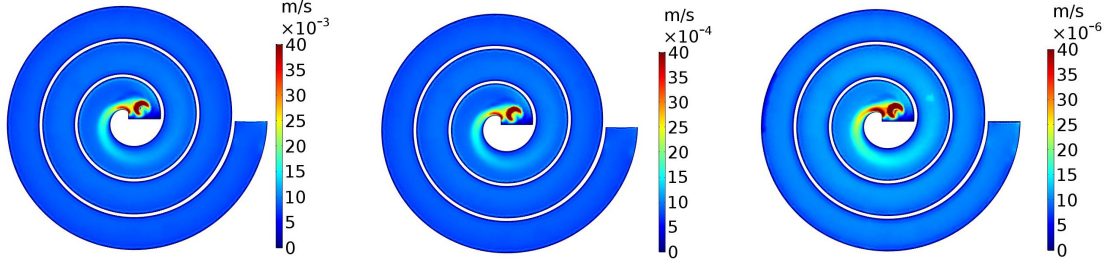
where Re is the Reynolds number, D_h is the hydraulic diameter, and R is the radius of curvature of the convex wall. The radius of curvature R at cross sections S1–S3 is equal to 0.02 m, 0.031 m and 0.044 m, approximately, while the channel has a rectangular cross section with base 0.01 m, height 7.6e-4 m and aspect ratio between the height and the width of the channel of 0.076. For configurations C1–C3, we estimated the Reynolds number using the average magnitude of the velocity in Ω_f computed by the NSD model with $\alpha = 1$. Table 6 reports the computed Reynolds and Dean numbers.

For all configurations C1–C3, the values of the Dean number are high enough according to [27] to indicate that vortices may have measurable effects on filtration. In Fig. 11, we clearly notice that vortices form both in the upper and in the lower part of the channel but in a non-symmetric way

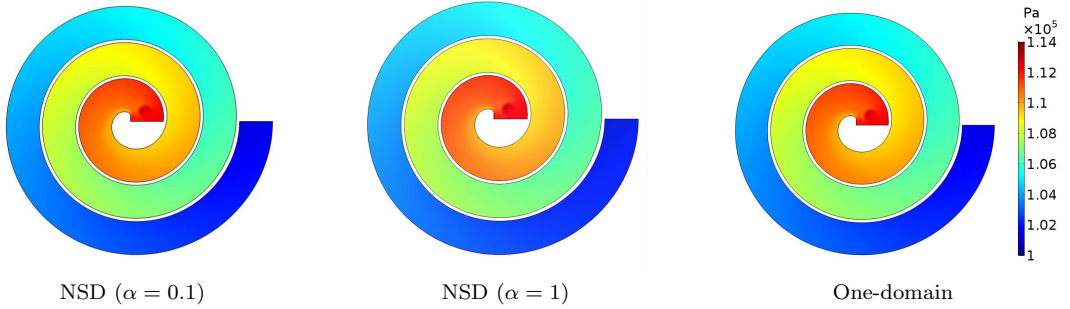
Magnitude of the normal velocity component:



Magnitude of the tangential velocity component:



Absolute pressure:



NSD ($\alpha = 0.1$)

NSD ($\alpha = 1$)

One-domain

Figure 6: Quantities of interest on the interface Γ_I ($z = 2.73\text{e-}4$ m) for configuration C2 and NSD with $\alpha = 0.1$ (left), $\alpha = 1$ (centre), and the one-domain model (right): normal velocity component (top), tangential velocity component (middle), absolute pressure (bottom).

due to the different imposed boundary conditions. Indeed, while on the top boundary a no-slip condition is prescribed for the velocity, the BJS condition on Γ_I (6) and the continuity of the normal velocity (4) result in a non-zero velocity in the neighbourhood of the membrane. Thus, the vortices near the interface tend to occupy a larger area than those at the top of the channel and they start forming at lower inflow pressure as it can be seen in configuration C1. The two types of vortices are expected to play a different role in the filtration process. While those in the upper part of the channel may favour the mixing of suspended particles, those that are closer to the fluid/porous-medium interface may contribute to disrupt solute build-up on the membrane surface, thus possibly increasing permeation rates. We remark that, as the magnitude of the velocity increases due to higher inflow pressure, the centre of maximum velocity shifts towards the concave wall as observed also, e.g., in [31]. The computational results and, in particular, the evidence of Dean vortices forming in the neighbourhood of the fluid/porous-medium interface support the experimental findings of [35] where a reduction in the concentration polarization effect was observed for our filtration system.

It is well-known that in rectangular cross-sectional curved channels with impermeable walls, the behaviour of Dean vortices depends on the aspect ratio of the channel [31, 38], with larger aspect ratios usually associated to the development of vortices at lower values of the Dean number than

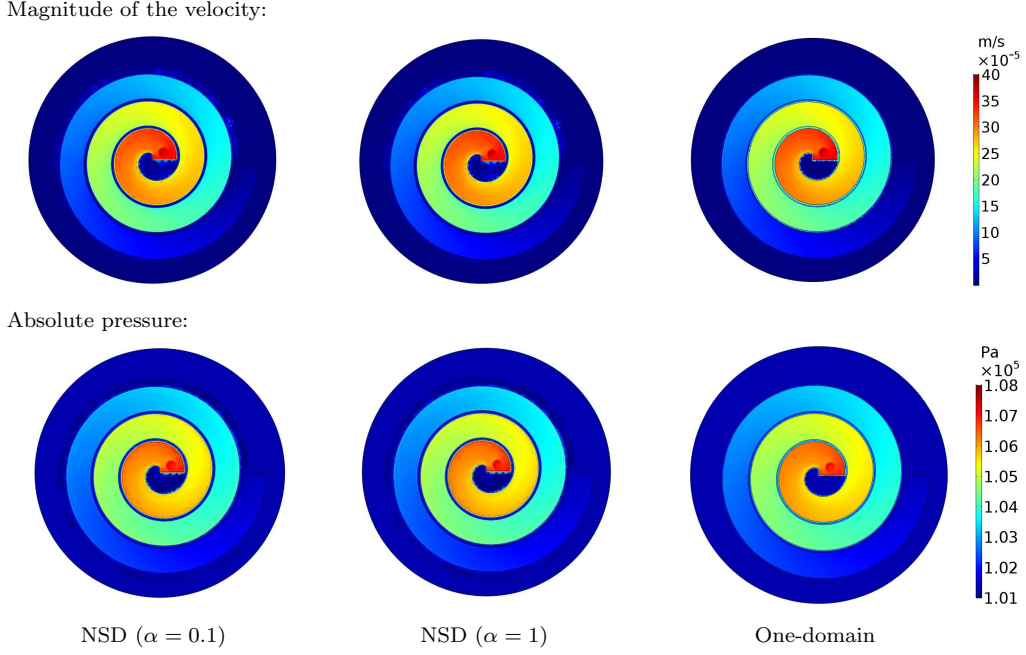


Figure 7: Quantities of interest in the middle of the membrane ($z = 1.365\text{e}-4$ m) for configuration C2 and NSD with $\alpha = 0.1$ (left), $\alpha = 1$ (centre), and the one-domain model (right): velocity (top), absolute pressure (bottom).

Table 6: Estimated Reynolds and Dean numbers for configurations C1–C3 at cross sections S1–S3. (Geometrical setting with aspect ratio 0.076.)

Configuration	C1	C2	C3
Reynolds Re	382.81	1474.53	5642.92
Dean De at S1	71.68	276.09	1056.57
Dean De at S2	57.30	220.70	844.58
Dean De at S3	48.32	186.14	712.34

in the case of smaller aspect ratios. We confirm a similar behaviour for the coupled fluid/porous-medium system that we are studying by considering a modified geometrical setting with cross-sectional aspect ratio 0.253 instead of the original one of 0.076. This is achieved by scaling the dimension of the filtration system in the radial direction by a factor 0.3 while keeping the vertical dimension unchanged. In this scaled setting, the inflow pressures of configurations C1–C3 result in larger Reynolds numbers than those observed in the original case as reported in table 7. Larger Re and reduced radius of curvature of the convex wall give larger Dean numbers at cross sections S1–S3, leading to the development of vortices already for configuration C1. This is clearly visible in Fig. 12 where we can see that vortices are present at the top of the channel and close to the membrane surface for all the inflow pressures considered here. These results suggest that adopting a system with a larger aspect ratio may provide better mixing of the feed and improved permeation rates already for low inflow pressures, with a clear advantage in terms of energy consumption.

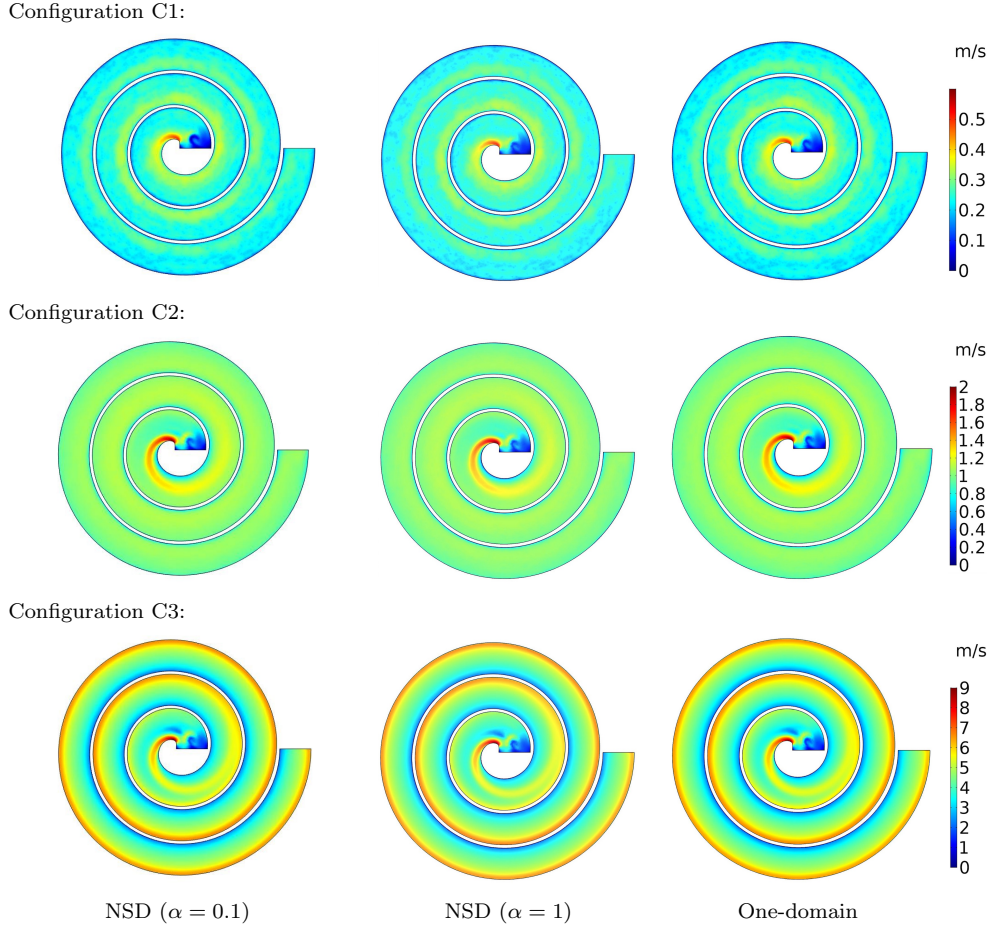


Figure 8: Magnitude of the velocity using the NSD and the one-domain models in the middle of the spiral channel ($z = 6.53\text{e}-4$ m) for configurations C1–C3.

5 Conclusion

We presented a mathematical and numerical framework to study the hydrodynamic behaviour of a novel membrane-based hybrid filtration system and to support experimental evidence. After numerically studying the impact of the modelling approach on the results of simulations, we identified Dean vortices and characterized them in terms of inflow pressure and aspect ratio of the channel. We discussed how the formation of these vortices could be favoured in order to enhance the filtration performance of the system without increasing the energy consumption. This study constitutes a first step towards the optimization of the water purification system and future work will look into incorporating models for suspended particles in the fluid.

Acknowledgements

The first author acknowledges the support of the EPSRC Doctoral Training Programme awarded to Loughborough University.

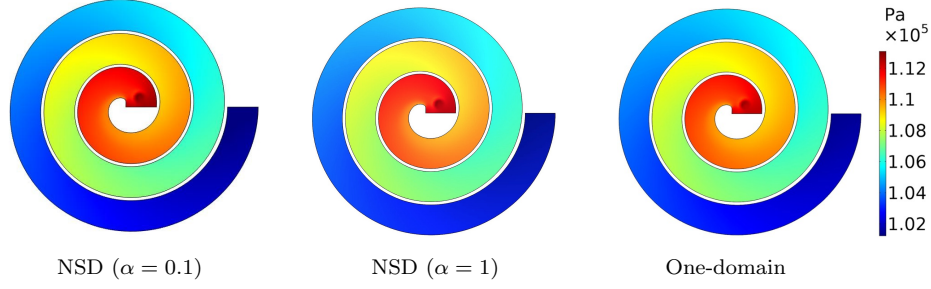


Figure 9: Absolute pressure computed using the NSD and the one-domain models in the middle of the spiral channel ($z = 6.53\text{e-}4$ m) for configuration C2.

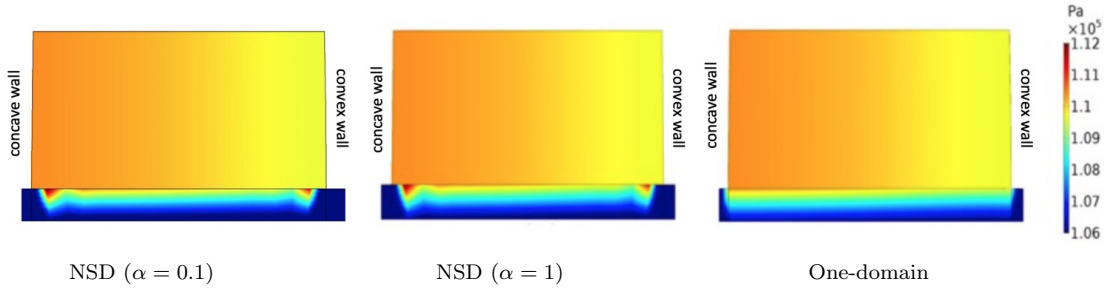


Figure 10: Absolute pressure for NSD and one-domain models at cross section S1 both in the fluid channel and inside the membrane for configuration C2. (For visualization, the horizontal axis has been scaled by a factor 0.15.)

References

- [1] P. R. Amestoy, I. S. Duff, J. Koster, and J. Y. L'Excellent. A fully asynchronous multifrontal solver using distributed dynamic scheduling. *SIAM J. Matrix Anal. Appl.*, 23(1):15–41, 2001.
- [2] P. Angot. Analysis of singular perturbations on the Brinkman problem for fictitious domain models of viscous flows. *Math. Methods Appl. Sci.*, 22(16):1395–1412, 1999.
- [3] P. Angot. On the well-posed coupling between free fluid and porous viscous flows. *Appl. Math. Lett.*, 24(6):803–810, 2011.
- [4] L. Badea, M. Discacciati, and A. Quarteroni. Numerical analysis of the Navier-Stokes/Darcy coupling. *Numer. Math.*, 115(2):195–227, 2010.
- [5] G. S. Beavers and D. D. Joseph. Boundary conditions at a naturally permeable wall. *J. Fluid Mech.*, 30:197–207, 1967.

Table 7: Estimated Reynolds and Dean numbers for configurations C1–C3 at cross sections S1–S3. Scaled geometrical setting with aspect ratio 0.253.

Configuration		C1	C2	C3
Reynolds Re		443.87	1700.54	7029.68
Dean De at	S1	141.11	540.61	2234.77
	S2	112.80	432.14	1786.39
	S3	95.14	364.48	1506.68

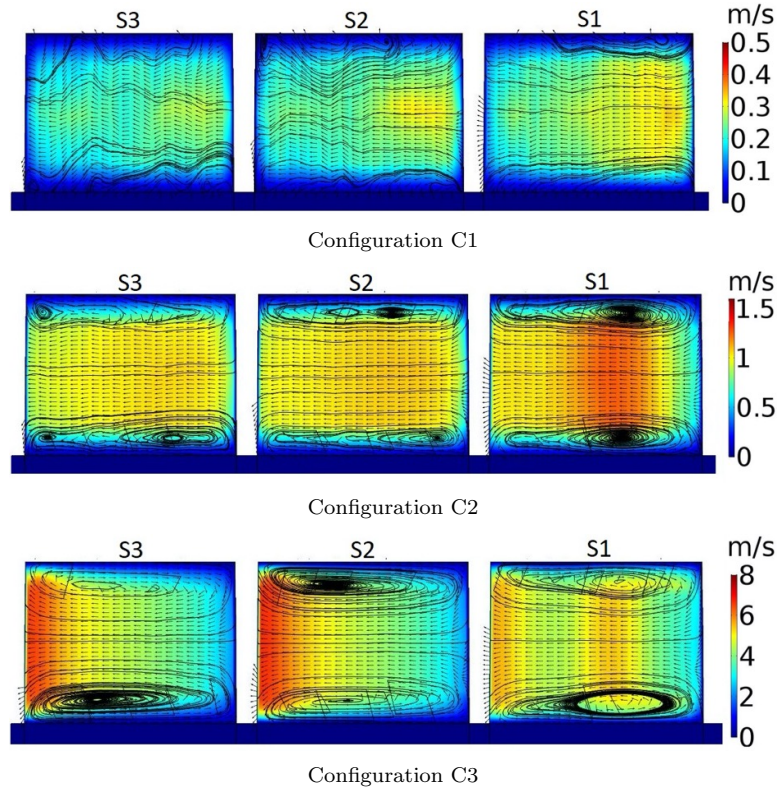


Figure 11: Velocity field and Dean vortices for NSD ($\alpha = 1$) for configurations C1–C3 at cross sections S1–S3 of the original geometry with aspect ratio 0.076. (For visualization, the horizontal axis has been scaled by a factor 0.1.)

- [6] S. A. Berger, L. Talbot, and L. S. Yao. Flow in curved pipes. *Annu. Rev. Fluid Mech.*, 15:461–512, 1983.
- [7] D. Boffi, F. Brezzi, and M. Fortin. *Mixed Finite Element Methods and Applications*. Springer, 2013.
- [8] H. C. Brinkman. A calculation of the viscous force exerted by a flowing fluid on a dense swarm of particles. *Appl. Sci. Res. A*, 1:27–34, 1947.
- [9] F. Cimolin and M. Discacciati. Navier-Stokes/Forchheimer models for filtration through porous media. *Appl. Numer. Math.*, 72:205–224, 2013.
- [10] H. Darcy. *Les Fontaines Publiques de la Ville de Dijon*. Dalmont, Paris, 1856.
- [11] D. B. Das and M. Lewis. Dynamics of fluid circulation in coupled free and heterogeneous porous domains. *Chem. Eng. Sci.*, 62:3549–3573, 2007.
- [12] W. R. Dean. Fluid motion in a curved channel. *Proc. R. Soc. London Ser. A-Math. Phys. Eng. Sci.*, 121(787):402–420, 1928.
- [13] J. E. Dennis and R. B. Schnabel. *Numerical Methods for Unconstrained Optimization and Nonlinear Equations*. SIAM, 1996.
- [14] P. Deuffhard. A modified Newton method for the solution of ill-conditioned systems of non-linear equations with application to multiple shooting. *Numer. Math.*, 22:289–315, 1974.

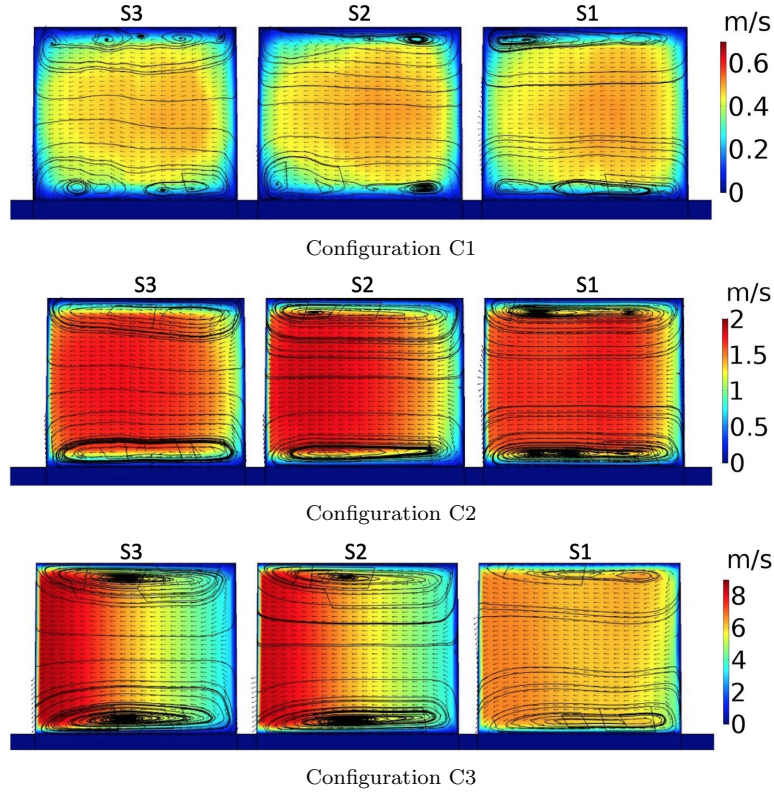


Figure 12: Velocity field and Dean vortices for NSD ($\alpha = 1$) for configurations C1–C3 at cross sections S1–S3 of the scaled geometry with aspect ratio 0.253. (For visualization, the horizontal axis has been scaled by a factor 0.3.)

- [15] M. Discacciati and A. Quarteroni. Navier-Stokes/Darcy coupling: modeling, analysis, and numerical approximation. *Rev. Mat. Complut.*, 22(2):315–426, 2009.
- [16] L. Durlofsky and J. F. Brady. Analysis of the Brinkman equation as a model for flow in porous media. *Phys. Fluids*, 30(11):3329–3341, 1987.
- [17] R. Ghidossi, D. Veyret, and P. Moulin. Computational fluid dynamics applied to membranes: State of the art and opportunities. *Chem. Eng. Process.*, 45:437–454, 2006.
- [18] V. Girault and B. Rivière. DG approximation of coupled Navier-Stokes and Darcy equations by Beaver-Joseph-Saffman interface condition. *SIAM J. Numer. Anal.*, 47:2052–2089, 2009.
- [19] B. Goyeau, D. Lhuillier, D. Gobin, and M. G. Velarde. Momentum transport at a fluid-porous interface. *Int. J. Heat Mass Transf.*, 46:4071–4081, 2003.
- [20] P. Hansbo and A. Szepessy. A velocity-pressure streamline diffusion finite element method for the incompressible Navier-Stokes equations. *Comp. Meth. Appl. Mech. Engrg.*, 84(2):175–192, 1990.
- [21] O. Iliev and V. Laptev. On numerical simulation of flow through oil filters. *Comput. Visual. Sci.*, 6(2):139–146, 2004.
- [22] COMSOL Inc. COMSOL Multiphysics version 5.3a. <https://www.comsol.com>.
- [23] R. Ingram. Finite element approximation of nonsolenoidal, viscous flows around porous and solid obstacles. *SIAM J. Numer. Anal.*, 49:491–520, 2011.

- [24] W. Jäger and A. Mikelić. On the boundary conditions at the contact interface between a porous medium and a free fluid. *Ann. Scuola Norm. Sup. Pisa Cl. Sci.*, 23:403–465, 1996.
- [25] K. Khadra, P. Angot, S. Parneix, and J. Caltagirone. Fictitious domain approach for numerical modelling of Navier-Stokes equations. *Int. J. Heat Mass Transfer*, 34:651–684, 2000.
- [26] M. Le Bars and M. Grae Worster. Interfacial conditions between a pure fluid and a porous medium: implications for binary alloy solidification. *J. Fluid Mech.*, 550:149–173, 2006.
- [27] P. Moulin, P. Manno, J. C. Rouch, C. Serra, M. J. Clifton, and P. Aptel. Flux improvement by Dean vortices: ultrafiltration of colloidal suspensions and macromolecular solutions. *J. Membr. Sci.*, 156:109–130, 1999.
- [28] J. Mulder. *Basic Principles of Membrane Technology*. Springer, 1996.
- [29] V. Nassehi and D. B. Das. *Computational Methods in the Management of Hydro-Environmental Systems*. IWA Publishing, 2007.
- [30] G. Neale and W. Nader. Practical significance of Brinkman’s extension of Darcy’s law: Coupled parallel flows within a channel and a bounding porous medium. *Can. J. Chem. Eng.*, 52(4):475–478, 1974.
- [31] N. Nivedita, P. Ligrani, and I. Papautsky. Dean flow dynamics in low-aspect ratio spiral microchannels. *Scientific Reports*, 7:44072, 2017. DOI: 10.1038/srep44072.
- [32] M. Paipuri, S. H. Kim, O. Hassan, N. Hilal, and K. Morgan. Numerical modelling of concentration polarisation and cake formation in membrane filtration processes. *Desalination*, 365:151–159, 2015.
- [33] K. M. Persson, V. Gekas, and G. Trägårdh. Study of membrane compaction and its influence on ultrafiltration water permeability. *J. Membr. Sci.*, 100:155–162, 1995.
- [34] P. G. Saffman. On the boundary condition at the interface of a porous medium. *Stud. Appl. Math.*, 1:93–101, 1971.
- [35] N. Shamsuddin, C. Cao, V. M. Starov, and D. B. Das. A comparative study between stirred dead end and circular flow in microfiltration of China clay suspensions. *Water Sci. Technol.-Water Supply*, 16(2):481–492, 2016.
- [36] N. Shamsuddin, D. B. Das, and V. M. Starov. Filtration of natural organic matter using ultrafiltration membranes for drinking water purposes: Circular cross-flow compared with stirred dead end flow. *Chem. Eng. J.*, 276:331–339, 2015.
- [37] J. Sogn. Stabilized finite element methods for the Brinkman equation on fitted and fictitious domains. Master’s thesis, University of Oslo, 2014.
- [38] S. Sugiyama, T. Hayashi, and K. Yamazaki. Flow characteristics in the curved rectangular channels (visualization of secondary flow). *Bull. JSME*, 26:964–969, 1983.
- [39] A. Ochoa Tapia and S. Whitaker. Momentum transfer at the boundary between a porous medium and a homogeneous fluid I. Theoretical development. *Int. J. Heat Mass Transfer*, 38:2635–2646, 1995.
- [40] K. Vafai and R. Thiyagaraja. Analysis of flow and heat transfer at the interface region of a porous medium. *Int. J. Heat Mass Transfer*, 30:1391–1405, 1987.